Experiments in Fluids (2021) 62:149
https://doi.org/10.1007/s00348-021-03240-5

RESEARCH ARTICLE

Measurements of trajectories and spatial distributions of diatoms (*Coscinodiscus* spp.) at dissipation scales of turbulence

Nimish Pujara[1,2] · Kevin T. Du Clos[3,4] · Stephanie Ayres[3] · Evan A. Variano[1] · Lee Karp-Boss[3]

Received: 13 December 2020 / Revised: 4 June 2021 / Accepted: 8 June 2021 / Published online: 3 July 2021
© The Author(s), under exclusive licence to Springer-Verlag GmbH Germany, part of Springer Nature 2021

Abstract

Diatoms are a group of photosynthetic microorganisms that play important roles in aquatic food webs and global biogeochemical cycles. They reside in the upper layer of oceans and lakes, and their interactions with the dissipation scales of turbulence govern a variety of processes, such as nutrient acquisition, prey–predator interactions, and aggregation. Interactions of cells with turbulence may also alter vertical motions and spatial distributions. However, observations of these interactions remain scarce because of the difficulty of generating ecologically relevant flows in the lab or tracking microscopic cells in the field. Here, we present an experimental system capable of measuring trajectories and spatial distributions of live diatom cells in turbulence. The small-volume turbulence tank uses stochastic forcing to restrict mean flow while producing homogeneous turbulence statistics at relatively high Reynolds number. Individual cell trajectories are tracked in three dimensions with a volumetric particle imager that uses the principle of defocused imaging combined with a double-pinhole aperture mask to obtain particle positions in three dimensions using a single camera. We conducted experiments at two different turbulence intensities and our results show that while root-mean-square velocities of diatoms are similar to those of tracer particles, their spatial distributions indicate enhanced clustering at the dissipation scales in comparison with tracer particles. This clustering behaviour is surprising both because diatom cells are characterised by a very low Stokes number and because clustering decreases when the turbulence intensity (and dissipation rate) increases. Several mechanisms could explain this result, including cell shape effects and active regulation of cell density in response to the ambient turbulence.

Graphic abstract

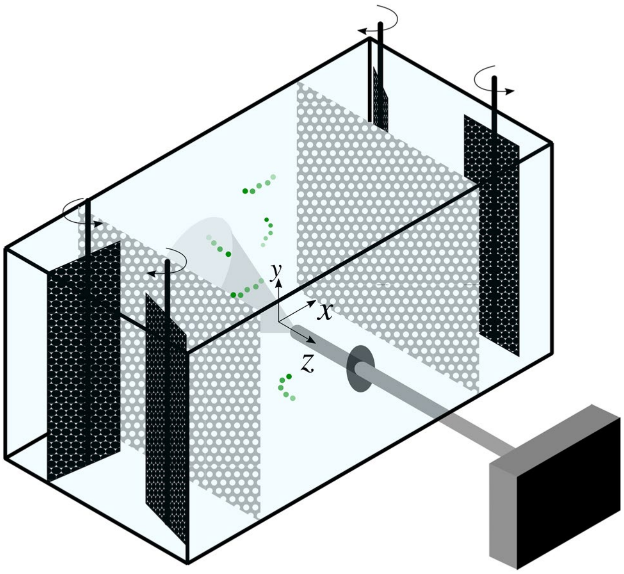

Extended author information available on the last page of the article

1 Introduction

Diatoms are key players in aquatic ecosystems, carrying out up to one-fifth of the photosynthesis on Earth, generating organic carbon that serves as the base of marine food webs, and playing a significant role in global biogeochemical cycles of carbon and silica (Armbrust 2009; Bowler et al. 2010; Ragueneau et al. 2006; Malviya et al. 2016). The upper layer of oceans and lakes, where diatoms reside, is characterised by turbulent flows, and interactions of diatoms with the ambient turbulence are central to understanding almost every aspect in the life of this important group of photosynthetic microorganisms. Diatoms cells lack flagella or cilia, which makes them non-motile, but their cell density slightly exceeds that of the surrounding water, and hence they tend to sink through the water column.

Observations in a Taylor–Couette device and an oscillating grid turbulence tank showed enhanced diatom settling velocities in turbulence relative to quiescent water (Ruiz et al. 2004). Trajectory biasing and preferential sweeping (Maxey 1987) were proposed as potential mechanisms to explain these observations. While recent numerical simulations of sinking diatoms in turbulence have shown evidence of trajectory biasing and the preferential sweeping mechanism for non-spherical body shapes (Niazi Ardekani et al. 2017), the overall effect was too small to explain the enhanced settling velocities reported in Ruiz et al. (2004).

Separately, experiments have shown that diatoms can actively alter their settling velocity in quiescent water in response to nutrient availability and local shear by regulating their buoyancy (Gemmell et al. 2016; Du Clos et al. 2019; Du Clos et al. 2021; Arrieta et al. 2020). Complementary numerical modelling has shown that such active regulation of buoyancy in response to turbulence-induced mechanical cues at the dissipation scales could result in clustering and alter settling velocities (Borgnino et al. 2019; Arrieta et al. 2020). When subjected to oscillating grid turbulence over extended periods of time, studies have also shown that chain-forming diatoms may alter their morphology (Amato et al. 2017; Dell'Aquila et al. 2017). Thus, while it is clear that diatoms can and do respond to both physical and chemical cues in their environment over multiple time scales, their response to turbulence is not well understood.

Experimental observations and measurements of live diatoms at the dissipation scales of turbulence are scarce because it is difficult to generate ecologically relevant flows in the lab and track motions of individual cells in three dimensions. Large-volume turbulence tanks are typically impractical for phytoplankton experiments because massive culturing efforts are required to get high numbers of cells that can be tracked to generate data with sufficient statistical power, while smaller turbulence tanks have difficulty generating high-Reynolds-number turbulence with homogeneous statistics. Additionally, turbulence tanks typically used for phytoplankton studies (oscillating grids and orbital shakers, Guadayol et al. 2009) are subject to strong mean flow patterns that make tracking of individual cells difficult and data prone to misinterpretation due to significant gradients in velocity and dissipation statistics.

Here, we fill this gap in experimental investigations of diatom cells in turbulence. We describe an experimental system with a small-volume turbulence tank that is capable of generating turbulent flow with low mean flow and homogeneous statistics at reasonable Reynolds numbers (Sect. 2), and a volumetric particle imager that is able to track individual diatom cells in three dimensions (Sect. 3). After presenting tests of particle trajectory analyses using synthetic data (Sect. 4), we report measurements and results with two species of diatoms and compare the statistics of trajectories and spatial distributions to those of tracer particles at two different turbulence intensities (Sect. 5). We find that turbulence induces a much greater clustering in the diatom cells than in tracer particles and that this difference in clustering diminishes when the turbulence intensity increases.

2 Turbulence tank

2.1 Tank design

We designed and constructed a small-volume turbulence tank made out of polycarbonate plastic that measures 12.25

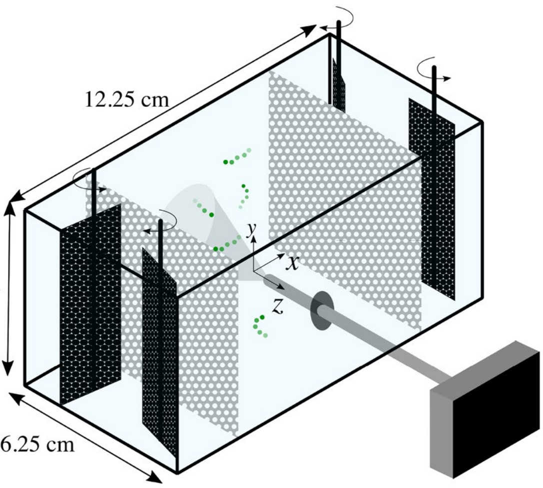

Fig. 1 Schematic diagram of turbulence tank and volumetric particle imager (VoPI)

cm (length) by 8.25 cm (height) by 6.25 cm (width), as shown in Fig. 1. Flow is generated in the tank by four rotating paddles in the four corners of the tank, where each paddle is a rigid mesh with square holes of side-length 2 mm. Each paddle is driven by a Lego Robotics motor (Model NXT, production year 2006, 9 VDC, 2 A, 0.5 Nm maximum torque). The paddles are separated from the central volume of the tank by 2 screens with an opening area ratio of 58% and holes of diameter 5 mm. The paddles and screens are acrylonitrile butadiene styrene (ABS) plastic, making the entire system metal free, nontoxic, and therefore suitable for studies with seawater and live organisms.

Flow in the tank is controlled by the number of paddles simultaneously in motion, the direction of rotation for each paddle, and the motor power level for each paddle. From systematic investigations of multiple stochastic algorithms, we found that the algorithm that produced the lowest mean flow relative to the turbulence intensity was the ‘figure-skating algorithm’: each paddle, operating independently of the others, rotates for a period of time T_{on1}, then switches direction and rotates in the opposite direction for a period of time T_{on2}, and then remains motionless for a period of time T_{off}. The parameters T_{on1}, T_{on2}, and T_{off} are all random numbers drawn from a uniform distribution spanning 1000–3000 ms.

We used the tank in two different modes of operation: a low-intensity (Low-Int) mode, where the motor power was 50% of its maximum value, and a high-intensity (High-Int) mode, where the motor power was at its maximum value.

2.2 Turbulence characteristics

To characterise the flow generated by the figure-skating algorithm in Low-Int and High-Int modes, we performed velocity measurements using stereoscopic particle image velocimetry (SPIV). The tank was filled with filtered water (Milli-Q) seeded with hollow glass spheres (diameter = 9–13 μm, ρ=1.10±0.05 g cm^{-3}, Sphericel, Potter Industries) that acted as tracer particles. We created a laser sheet of 1 mm nominal thickness in the $x-y$ plane with a pulsed Nd:YAG laser (emission wavelength of 532 nm; New Wave Research) and took images from two stereoscopically arranged Imager Intense cameras (1376 × 1040 pixel resolution) that were operated in double-frame mode with a frame separation time (dt) of 8 ms. Images were processed using DaVis v8 software (LaVision), where the first pass was performed using sub-windows of 64 × 64 px, followed by three passes at 32 × 32 px. Velocity data were taken at a rate of 0.5 Hz for 1200 s, which resulted in 600 independent snapshots of the velocity field for ensemble averaging.

We took SPIV data in $x-y$ planes at different z values (z = 0, ±1, and ±2 cm) to check the sensitivity of flow statistics to wall effects. We did not observe strong variations within this observation volume, and therefore, only present results from the $z=0$ plane here.

One-point statistics and mean flow To analyse SPIV velocity data, we decompose the velocity into a mean and fluctuating quantity using a Reynolds decomposition:

$$\mathbf{u} = \langle \mathbf{u} \rangle + \mathbf{u}', \tag{1}$$

where $\langle \mathbf{u} \rangle$ is the ensemble mean velocity (calculated by averaging over time) and $\mathbf{u}'$ is the turbulent fluctuation. The root-mean-square (RMS) values for the turbulent fluctuations of each component quantify the strength of the turbulence velocity in each direction, and we define an overall turbulence velocity scale as: $u_{\mathrm{RMS}} = \left[(\langle u'^2 \rangle + \langle v'^2 \rangle + \langle w'^2 \rangle)/3\right]^{1/2}$. Spatially averaged values of u_{RMS} and RMS values of each component are given in Table 1.

Spatial variation of mean and root-mean-square velocities (Fig. 2) show that the central region of the tank has low mean flow and relatively homogeneous turbulent velocity fluctuations. The turbulent velocity fluctuations show a degree of anisotropy with the $\langle u'^2 \rangle^{1/2}$ and $\langle w'^2 \rangle^{1/2}$ being larger than $\langle v'^2 \rangle^{1/2}$, likely due to the paddle forcing generating velocities predominantly in the $x-z$ plane. To quantify the strength of the mean flow relative to the turbulent fluctuations, we follow Variano and Cowen (2008) and calculate the ratios $\mathbf{M} = |\langle \mathbf{u} \rangle| / \mathbf{u}_{\mathrm{RMS}}$ and $M^* = (\langle u \rangle^2 + \langle v \rangle^2 + \langle w \rangle^2)/(\langle u'^2 \rangle + \langle v'^2 \rangle + \langle w'^2 \rangle)$. Spatially averaged values of $\mathbf{M}$ and M^* are listed in Table 1 and demonstrate that mean flow is weak compared with turbulent fluctuations under both modes of tank operation.

An important consideration when studying the effects of turbulence on the mean settling velocity of particles is the

Table 1 Parameters of turbulent flow

	Low-Int	High-Int
$\langle u'^2 \rangle^{1/2}$ (mm/s)	7.0	18.7
$\langle v'^2 \rangle^{1/2}$ (mm/s)	4.6	14.9
$\langle w'^2 \rangle^{1/2}$ (mm/s)	8.0	32.3
u_{RMS} (mm/s)	6.5	21.7
M_1	0.052	0.028
M_2	0.461	0.047
M_3	0.024	0.005
M^*	0.098	0.018
$\langle \epsilon \rangle$ (mW/kg)	0.0069	0.16
η (mm)	0.62	0.28
τ_η (ms)	381	78
u_η (mm/s)	1.6	3.6
λ (mm)	9.8	6.6
L (mm)	25.2	22
ReL	164	480
Re_λ	64	142

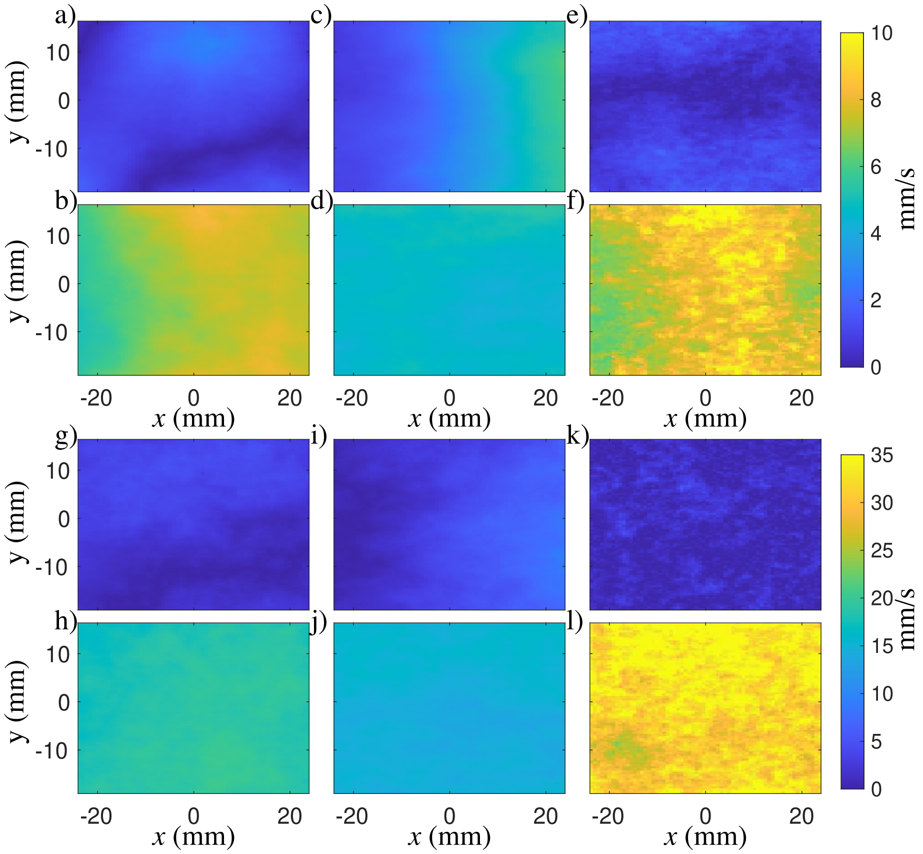

Fig. 2 One-point statistics for Low-Int mode (**a–f**) and High-Int mode (**g–l**). Panels in the top row for each mode are absolute values of the mean velocity: $|\langle u\rangle|$ (**a, g**); $|\langle v\rangle|$ (**c, i**); $|\langle w\rangle|$ (**e, k**). Panels in the bottom row for each mode are the RMS values of the turbulent fluctuations: $\langle u'^2\rangle^{1/2}$ (**b, h**); $\langle v'^2\rangle^{1/2}$ (**d, j**); $\langle w'^2\rangle^{1/2}$ (**f, l**)

structure of the mean flow. The mean flow in our tank does not have a stationary structure as shown by splitting the 600 snapshots of the velocity field into three equal time segments and calculating the mean flow for the first (Fig. 3a, d) and the last segment (Fig. 3b, e). The difference in mean flow between the first and last segments is of the same order as the mean flow itself (Fig. 3c, f). Previous investigations have found that stochastic forcing continually disrupts tank-scale recirculations, helping to lower the magnitude of the mean flow (Variano and Cowen 2008; Pérez-Alvarado et al. 2016). Here, we also show this produces a non-stationary mean flow.

Two-point statistics We characterise the spatial structure of turbulence using two-point statistics. We calculate the spatial correlation functions:

$$a(s)_{ij,k} = \frac{\langle u_i'(\mathbf{x}) \cdot u_j'(\mathbf{x} + s\, e_k)\rangle}{\left(\langle u_i'\rangle^2 \langle u_j'\rangle^2\right)^{1/2}}, \tag{2}$$

and the second-order structure functions:

$$D_{ij,k}(s) = \left\langle \left(u_i'(\mathbf{x}) - u_j'(\mathbf{x} + s\, e_k)\right)^2 \right\rangle, \tag{3}$$

in which s is the spatial lag and e_k is the unit vector in the direction in which the spatial lag is taken (Pope 2000).

We calculate the mean turbulent energy dissipation rate, $\langle\epsilon\rangle$, by using Kolmogorov theory (1941a; b; K41), which states that $D_{LL} = C_2(\langle\epsilon\rangle s)^{2/3}$ in the inertial subrange, where D_{LL} is the longitudinal structure function and $C_2 = 2.0$ is the Kolmogorov constant (Pope 2000). We estimate the extent of the inertial subrange via the compensated longitudinal structure function, $s^{-1}D_{11,1}^{3/2}$, with the inertial subrange being where the value of $s^{-1}D_{11,1}^{3/2}$ is within 5% of its maximum value. The mean dissipation rate is then calculated with the average value of $D_{11,1}$ over this inertial subrange using $\langle\epsilon\rangle = s^{-1}(D_{11,1}/C_2)^{3/2}$ (Fig. 4a, c), which gives 6.9×10^{-6} W/kg and 1.6×10^{-4} W/kg for the Low-Int and High-Int modes, respectively (Table 1).

Based on the mean dissipation rates, we calculate the Kolmogorov (dissipation) scales via the relations:

$$\eta = (\nu^3/\langle\epsilon\rangle)^{1/4}, \tag{4a}$$

$$\tau_\eta = (\nu/\langle\epsilon\rangle)^{1/2}, \tag{4b}$$

$$u_\eta = (\nu\langle\epsilon\rangle)^{1/4}, \tag{4c}$$

where η, τ_η, and u_η are the Kolmogorov length, time, and velocity scales, respectively, and ν is the kinematic viscosity. These scales are given in Table 1.

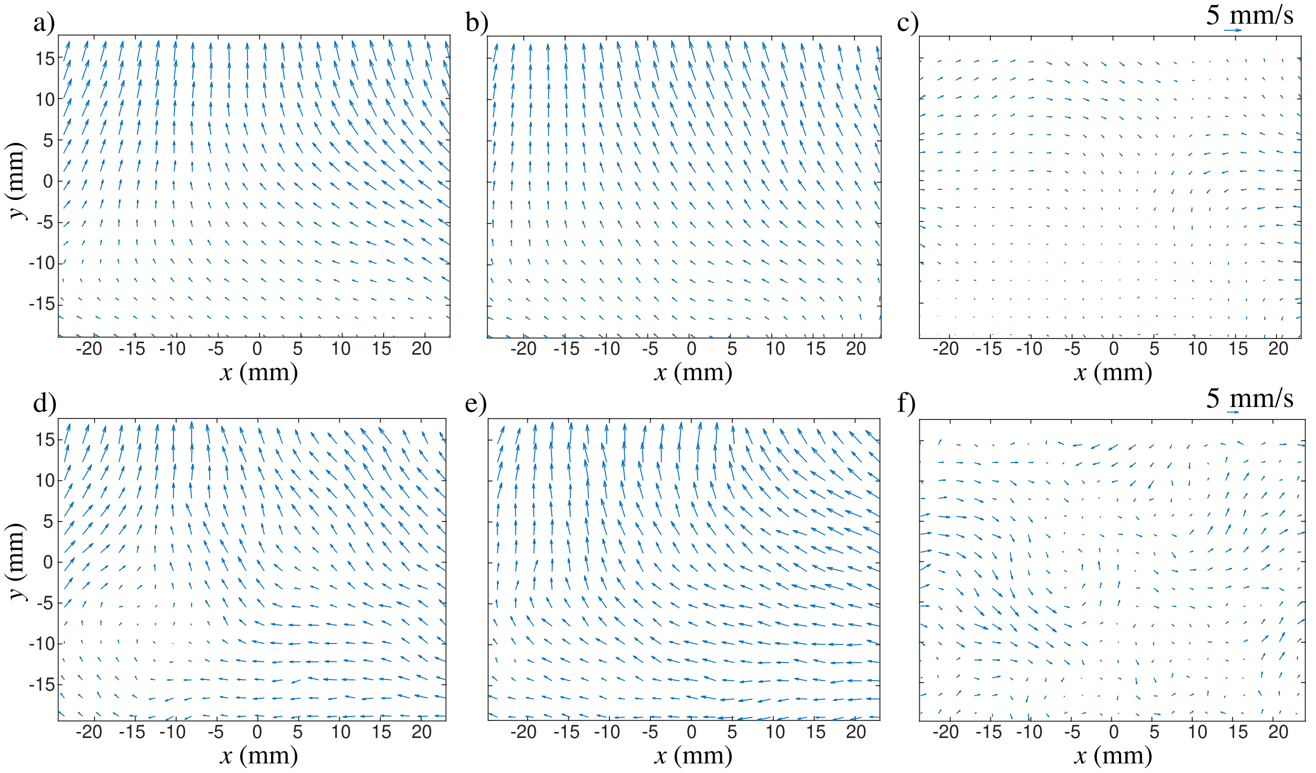

Fig. 3 Mean flow ($\langle u \rangle$,$\langle v \rangle$) in the $z = 0$ plane for Low-Int mode (**a**–**c**) and High-Int mode (**d**–**f**). Left panels (**a**, **d**) show mean flow for first segment of data, middle panels (**b**, **d**) show mean flow for last segment of data, and right panels (**c**, **f**) show the differences between the first and last segments of data. Scales shown in **c** and **f** are consistent over their respective rows

Fig. 4 Two-point statistics for Low-Int mode (**a**, **b**) and High-Int mode (**c**,**d**). Left panels (**a**, **c**) show the compensated second-order structure function (solid line) used to calculate mean dissipation rate. Right panels (**b**, **d**) show the spatial correlation function (solid line), a parabola fit near $s = 0$ to compute the Taylor scale (dashed line), and a model function (Eq. (G19) in Pope 2000) fit in the inertial subrange to calculate the integral scale (dashed-dotted line). Dotted vertical lines indicate the inertial subrange. In panel **b**, only the lower bound of the inertial subrange is shown

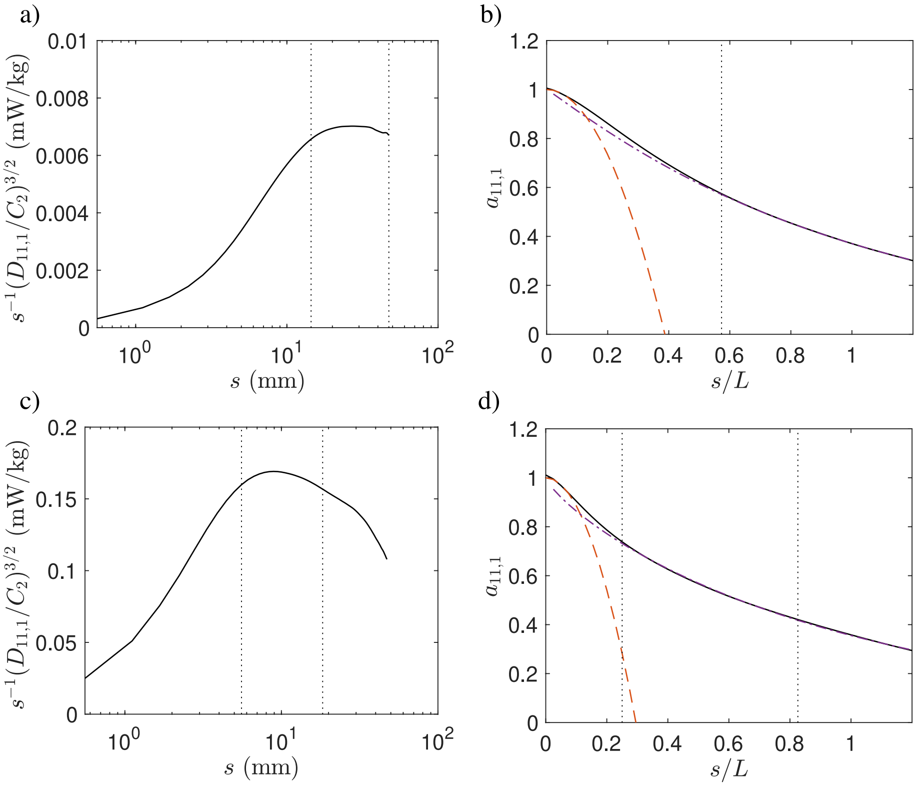

We also calculate the Taylor length scale and the integral length scale from the spatial correlation function. We fit an osculating parabola to the first 3 points of $a_{11,1}(s)$, excluding the point at $s = 0$, and find the Taylor scale, λ, as the positive root of this parabola (Eq. (6.53) in Pope 2000) (Fig. 4b, d). This gives Taylor length scales of $\lambda = 9.8$ mm (Low-Int) and $\lambda = 6.6$ mm (High-Int) and Reynolds numbers based on the Taylor length scale of $\mathrm{Re}_\lambda = 64$ (Low-Int mode) and $\mathrm{Re}_\lambda = 142$ (High-Int) (Table 1). These Re_λ values indicate that the flow is in the fully developed turbulence regime typical of laboratory experiments and direct numerical simulations. The spatial extent of the SPIV field of view was not sufficiently large to calculate the integral length scale directly via computing the integral

$$L_{ij,k} = \int_0^\infty a(s)_{ij,k}\,\mathrm{d}s. \tag{5}$$

Thus, following Bellani and Variano (2014), we fit a model of the correlation function in the inertial subrange where the integral length scale is a fitting parameter (Eq. (G.19) in Pope 2000) (Fig. 4b, d). This gives integral length scales of $L = 25.2$ mm (Low-Int) and 22 mm (High-Int) (Table 1).

We further investigate the scale-dependent turbulence structure in the flow by comparing different second-order structure functions and spatial correlation functions (Fig. 5). The longitudinal structure functions ($D_{11,1}$ and $D_{22,2}$) show that flow stretching in the Low-Int mode occurs more in the x-direction than the y-direction at all scales, but this difference diminishes in the High-Int mode. The corresponding spatial correlation functions ($a_{11,1}$ and $a_{22,2}$) show that the integral scale is smaller in the y-direction than the x-direction, but this difference is again reduced in the High-Int mode compared to the Low-Int mode. The transverse structure functions quantifying flow rotations about z-direction ($D_{11,2}$ and $D_{22,1}$) show that the flow anisotropy observed in the one-point statistics is present at all scales. $D_{11,2}$ is larger than $D_{22,1}$ in both Low-Int and High-Int modes. This behaviour is also reflected in the corresponding spatial correlation functions ($a_{11,2}$ and $a_{22,1}$), which show that the u velocity stays correlated with itself over a larger distance in the y-direction compared to the v velocity in the x-direction. Overall, the turbulence structure is weakly anisotropic.

3 Volumetric particle imager

Overview We used the volumetric particle imager (VoPI; Tse and Variano 2013) to take Lagrangian data of particle positions and velocities in the turbulence tank. Briefly, the VoPI measures 3D positions of particles within its measurement volume using the principle of defocused imaging (Willert and Gharib 1992; Pereira and Gharib 2002). Images are taken with a borescope (Pro Hardy 12″, 0.25” diameter, Gradient Lens Corporation) that is coupled to a digital camera (Prosilica GE680, Allied Vision Technologies) via a double-pinhole aperture mask. The measurement volume is lit with white light (Luxxor 24W LS, Gradient Lens Corporation)

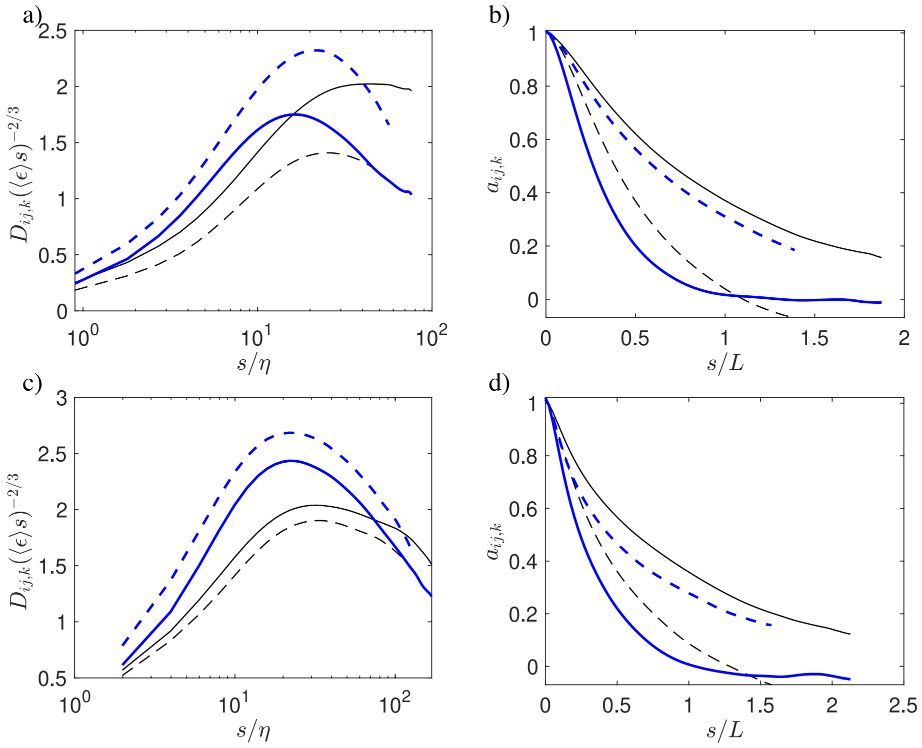

Fig. 5 All two-point statistics for Low-Int mode (**a**, **b**) and High-Int mode (**c**, **d**). Left panels (**a**, **c**) show the compensated second-order structure functions: $D_{11,1}$ (solid black line), $D_{22,2}$ (dashed black line), $D_{22,1}$ (thick solid blue line), and $D_{11,2}$ (thick dashed blue line). Right panels (**b**, **d**) show the spatial correlation functions: $a_{11,1}$ (solid black line), $a_{22,2}$ (dashed black line), $a_{22,1}$ (thick solid blue line), and $a_{11,2}$ (thick dashed blue line)

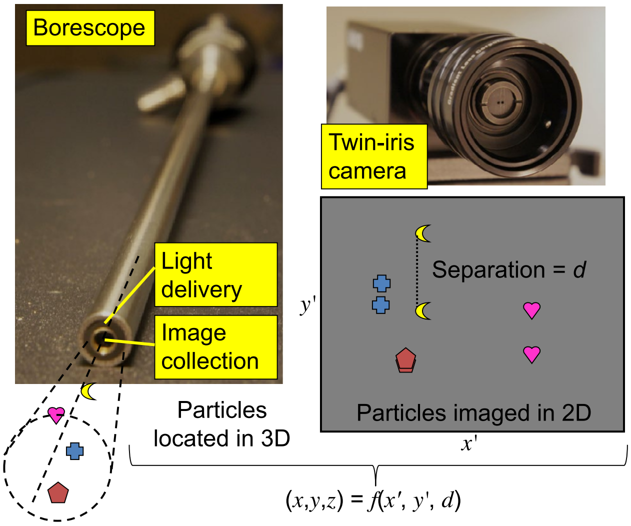

Fig. 6 VoPI components and an overview of 3D particle position measurements

that is delivered though optical fibres around the edge of the borescope. Figure 6 shows the VoPI and provides an overview of its concept, with further details available in Tse and Variano (2013). Here, we focus on the updates to its calibration and data analyses.

Image processing summary In the images collected by the VoPI camera, each particle appears as 2 objects (or a 'doublet') due to the double pinhole in the aperture mask. The image processing algorithm removes the background noise, identifies doublets, and calculates the location of the doublet centre (x', y'), separation distance between objects in a doublet d, widths of the 2 objects in the doublet (x'_w, y'_w), and intensity of the doublet (m) using user-defined thresholds. The separation distance, d, is computed by identifying the secondary peak in the autocorrelation function of the doublet (see Fig. 6 and accompanying text in Tse and Variano 2013 for a detailed description).

Calibration Doublet data in image coordinates (x', y', d) are converted to a 3D particle position in the laboratory frame (x, y, z) via calibration functions. We determined these calibration functions using calibration data acquired by taking repeated images of a calibration plate at different distances away from the borescope tip. The calibration plate consisted of a matrix of 0.15-mm-diameter dots separated by a known distance (0.5 or 1 mm, depending on the setting of the boroscope) with a reference dot marked for ease of orientation. We mounted the calibration plate perpendicular to the axis of the boroscope on a XY microstage for precise control of its distance from the boroscope. Starting with the calibration plate just touching the distal tip of the boroscope, we moved the tip of the boroscope away from the plate in increments of 1 mm, taking a new image each time. This calibration procedure was performed in seawater to match refractive indices of the media for experiments with phytoplankton cells in the turbulence tank. We fitted this data to the following calibration functions for in-plane (x, y) and out-of-plane (z) particle positions:

$$x = C_1 + C_2x' + C_3d + C_4x'd, \tag{6a}$$

$$y = C_1 + C_2y' + C_3d + C_4y'd, \tag{6b}$$

$$z = -C_5 \exp\left(-\frac{r^4}{C_6}\right) d^{C_7}. \tag{6c}$$

Here, (x, y, z) is the dot position relative to the VoPI's distal tip in the laboratory coordinate system, $r = \sqrt{(x^2 + y^2)}$ is the radial distance from the borescope axis, and C_1–C_7 are calibration coefficients. Since these calibration coefficients are unique to the borescope's focal setting, the VoPI only needs to be calibrated once.

We performed the calibration procedure for two different focal settings, which we call 'A' (a higher optical magnification to allow imaging of tracer particles of size $\approx 10\,\mu$m) and 'E' (a lower optical magnification to allow imaging of diatoms of size $\approx 100\,\mu$m). The calibration data and calibration functions are shown in Fig. 7 with values of calibration coefficients given in Table 2.

When using the VoPI in turbulence tank experiments, we exclude data that fall outside the measurement volume as defined by the convex hull of the calibration data of each focal setting. Thus, the calibration fits are not extended beyond the data originally used to generate them and the uncertainty in experimental data is characterised by the RMS values of the errors in the calibration data. This uncertainty is greatest in the z-position and increases slightly with distance away from the distal tip.

Particle tracking To obtain Lagrangian statistics from data of particle positions in each frame, we implemented a particle-tracking algorithm. We use the 4-frame best-estimate (4BE) algorithm in Ouellette et al. (2006), which is summarised in their Fig. 8. Briefly, this algorithm uses the nearest-neighbour heuristic from two consecutive frames to start building tracks and uses a 4-frame method to continue each track. The 4-frame method seeks candidate particles for a track within a predefined search radius of the predicted location in the next frame. Of all particles that match this criterion, the particle that is chosen to be part of the track is the one that finds a particle closest to the predicted location in the fourth frame, where this predicted location is calculated with finite-difference estimates of velocity and acceleration from the particle positions over the first three frames. We set the search radius to 0.5 mm

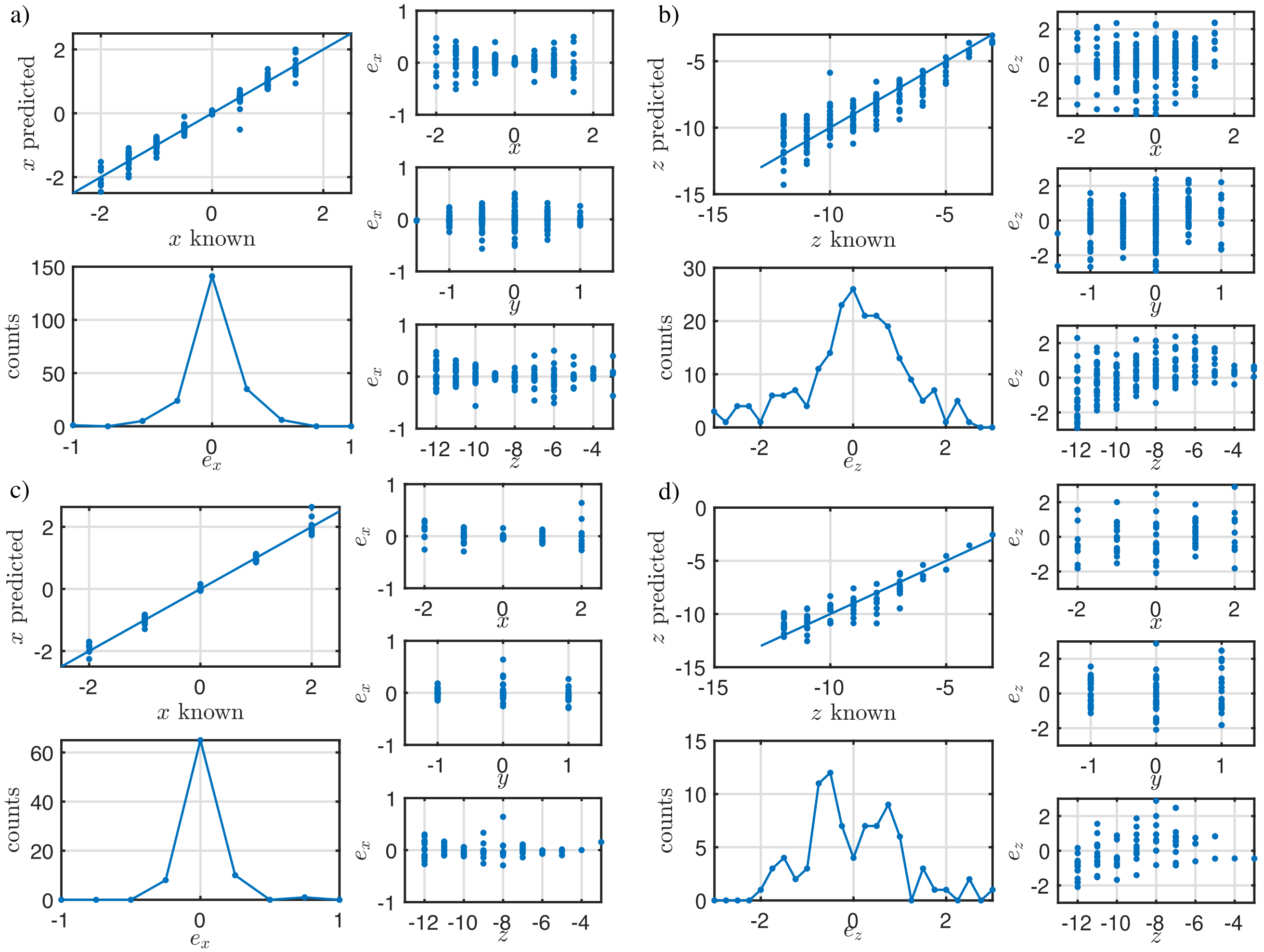

Fig. 7 Calibration data and errors associated with measuring particle position for focal setting ‘A’ x-positions (**a**), focal setting ‘A’ z-positions (**b**), focal setting ‘E’ x-positions (**c**), and focal setting ‘E’ z-positions (**d**). Positions (x and z) and errors in predicting those predictions (e_i) are in units of mm. Data for y is similar to that for x

in the x and y directions and 2.5 mm in the z direction, following the recommendation by Malik et al. (1993) to use (3 × expected particle displacement) + (3 × uncertainty in particle position). The performance of this particle tracking method is quantified in Sect. 4.

Particle velocity To calculate the Lagrangian particle velocities, we convolve the particle positions along their trajectories with a kernel that simultaneously performs Gaussian smoothing and differentiation (Mordant et al. 2004; Ouellette et al. 2006):

$$k(\tau) = \frac{\tau \exp\left(-\frac{\tau^2}{f_w^2}\right)}{\left[f_L f_w^2 \exp\left(-\frac{f_L^2}{f_w^2}\right) - \frac{f_w^3}{2}\sqrt{\pi}\,\mathrm{erf}\left(\frac{f_L}{f_w}\right)\right]}, \qquad (7)$$

with the filter width $f_w = 1$ frame and the filter support $f_L = 3$ frames. These filter parameters provide a good compromise between smoothing and minimum required track length ($2f_L$) while still ensuring that numerical convolution with a constant or a line of constant slope produce the expected results to within 1%.

We calculate statistics of particle velocity, such as mean and variance, from the particle velocities along their trajectories. Using all velocity samples from Lagrangian particle velocity data to calculate Eulerian velocity statistics results in biased values since slower particles produce longer tracks and hence more data (e.g., Buchhave et al. 1979). We avoid this bias by first computing averages for each track and then averaging across all tracks so that each track contributes equally regardless of its length. 95% confidence intervals are calculated by applying the bootstrap technique to this procedure with randomly selected tracks.

Clustering Particle clustering is typically quantified using the radial distribution function (RDF; e.g., Salazar et al. 2008). However, computing the RDF was not possible for our data because: (1) particle concentrations (number

Table 2 Parameters of the volumetric particle imager (VoPI) calibration with with 95% confidence intervals in brackets

	Focal setting 'A'	Focal setting 'E'
Measurement volume (mm^3)	38.8	40.7
Calibration coefficients for *x*-position (Eq. 6a)		
C_1	−3.57 [−3.73 −3.42]	−4.74 [−5.00 −4.47]
C_2	0.0104 [0.0100 0.0109]	0.0147 [0.0139 0.0154
C_3	0.0503 [0.0442 0.0564]	0.0777 [0.0684 0.0871]
C_4	−1.45 [−1.63 −1.28] ($\times 10^{-4}$)	−2.42 [−2.71 −2.13] ($\times 10^{-4}$)
Calibration coefficients for *y*-position (Eq. (6b))		
C_1	2.85 [2.72 2.99]	3.49 [3.09 3.88]
C_2	−0.0109 [−0.0114 −0.0105]	−0.0131 [−0.0147 −0.0115]
C_3	−0.0433 [−0.0485 −0.0380]	−0.0514 [−0.0655 −0.0374]
C_4	1.58 [1.39 1.76] ($\times 10^{-4}$)	1.93 [1.35 2.51] ($\times 10^{-4}$)
Calibration coefficients for *z*-position (Eq. 6c)		
C_5	87.29 [71.3 103]	252 [127 376]
C_6	100 [54.4 147]	135 [67.6 202]
C_7	−0.754 [−0.816 −0.692]	−0.993 [−1.14 −0.844]
Uncertainties in particle position		
$e_{x,\mathrm{RMS}}$ (mm)	0.17	0.13
$e_{y,\mathrm{RMS}}$ (mm)	0.12	0.14
$e_{z,\mathrm{RMS}}$ (mm)	1.1	1.0

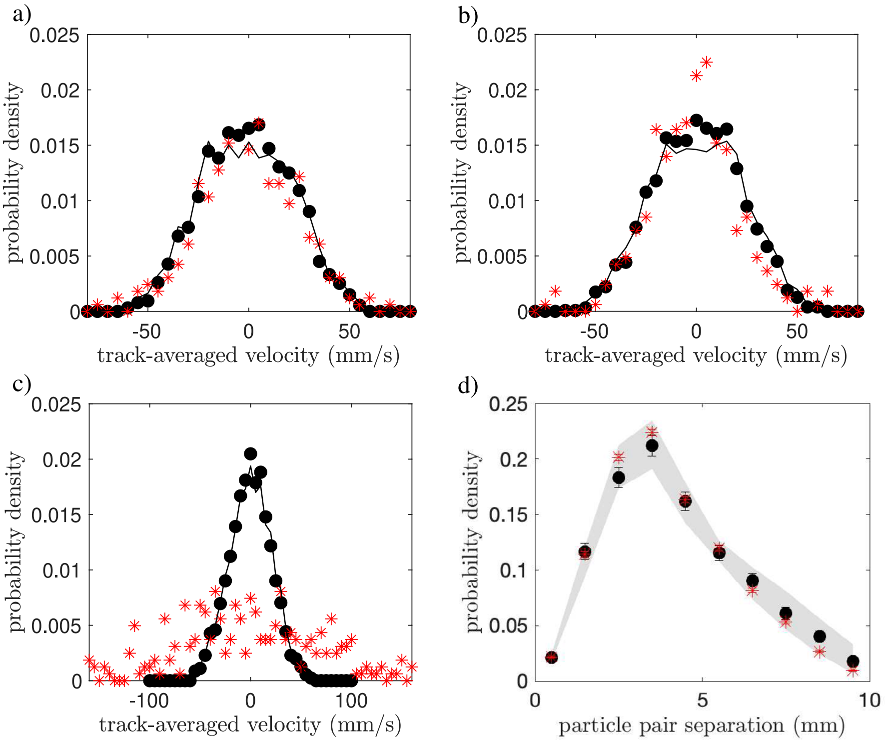

Fig. 8 Synthetic data analysis showing PDF of track-averaged velocities for **a** the *u* component, **b** *v* component, **c** *w* component, and **d** the clustering analysis. Black circles are analysis of noiseless data and red asterisks are analysis of noisy data. In panels **a**–**c**, the solid line is the distribution from the OU process. In panel d, the shaded region shows the 95% confidence intervals for the no-clustering scenario

of particles per unit volume) were intentionally kept low to avoid particle–particle interactions, which meant that individual frames contained insufficient data to compute the RDF; and (2) the RDF is a function of the measurement volume, which in our case was anisotropic and did not have periodic boundary conditions, making it difficult to normalise the histograms of particle-pair separation distances without introducing *ad hoc* assumptions. Instead of using the RDF, we quantified particle clustering by computing a probability density function (PDF) of pair-wise particle separation distances, with 95% confidence intervals computed using the bootstrap technique (Efron and Tibshirani 1993). These PDFs were computed for the data (excluding cases when tracks overlapped) and compared to a Monte Carlo simulation of the PDF expected for a case of no clustering. To generate the Monte Carlo simulation data of particles that uniformly sample the measurement volume, we drew samples of particle positions from a uniform distribution in a square box and excluded particles outside the VoPI's measurement volume so that the size and shape of our measurement volume were taken into account. We also matched the number of particles in the Monte Carlo simulation to the real data. We generated many sample sets to compute 95% confidence intervals of this no-clustering PDF. If particles were to cluster, the PDFs of pair-wise distances for the data would lie outside the range of the no-clustering Monte Carlo PDFs.

4 Synthetic data

Before describing the experiments with diatoms and tracer particles in the turbulence tank and their results, we first describe the generation and analysis of a synthetic dataset that replicates the type of data we gather in the experiments. This allows us to demonstrate the ability of our data analysis algorithms to accurately reproduce known statistics of particle velocity and clustering.

We generated synthetic particle tracks by modelling the Lagrangian velocity using an Ornstein–Uhlenbeck (OU) process, where each component of velocity is independent and evolves according to (Gillespie 1996):

$$U^*(t+\mathit{\Delta} t) = U^*(t)e^{-(\mathit{\Delta} t/T_\mathrm{L})} + nU^*_\mathrm{RMS}\left[1-e^{-(2\mathit{\Delta} t/T_\mathrm{L})}\right]^{1/2}, \quad (8)$$

where $U^*(t)$ is the Lagrangian velocity time series, $\mathit{\Delta} t$ is the time step, T_L is the Lagrangian integral scale, n is a random number drawn from a Gaussian distribution with zero mean and unit variance, and U^*_RMS is the RMS velocity. The OU process produces a Gaussian one-time PDF of velocity and an exponential Lagrangian velocity autocorrelation function. Overall, these properties compare reasonably well with data from moderate Reynolds number turbulence (pp. 485 in Pope 2000). Parameters of the synthetic data were chosen to match the parameters of our system in High-Int mode: $U^*_\mathrm{RMS} = 20$ mm/s; $T_\mathrm{L} = 1$ s; $\mathit{\Delta} t = 0.005$ s. Velocity time series for each velocity component were integrated using a 2^nd-order Runge–Kutta algorithm to give particle positions for each track. We generated 100,000 such tracks in a 3D cube of size 100 mm with periodic boundary conditions and then used data for tracks that entered a cuboid measurement volume of side length 2 mm and height 10 mm in the centre of the cube, which approximated the measurement volume of the VoPI. To understand the effects of measurement noise, we added Gaussian random noise to the particle positions in the synthetic dataset with a noise structure that mimicked the VoPI measurement noise ($e_{x,\mathrm{RMS}} = e_{y,\mathrm{RMS}} = 0.15$ mm, $e_{z,\mathrm{RMS}} = 1$ mm; Table 2). The noiseless and noisy synthetic data were fed into the data analysis pipeline to evaluate the performance of each step.

Defining a correctly recovered track as one that begins at the same frame as the synthetic data tracks and contains no spurious particles but may end earlier (Ouellette et al. 2006), the particle-tracking algorithm correctly recovered 97.6% of the tracks in the noiseless data, whereas it performed poorly in the noisy data because tracks never began at the same frame as the synthetic data tracks. The velocity PDFs calculated from particle tracks showed that the noiseless data matched the synthetic data closely for all components of velocity, whereas the noisy data matched the synthetic data only for the u and v components for which the noise levels were lower (Fig. 8a–c). For the noiseless data, the RMS particle velocities and their 95% confidence intervals were $\langle u^2\rangle^{1/2} = 22.2 \pm 0.5$ mm/s, $\langle v^2\rangle^{1/2} = 21.9 \pm 0.5$ mm/s, and $\langle w^2\rangle^{1/2} = 20.8 \pm 0.5$ mm/s, whereas for the noisy data the corresponding values were $\langle u^2\rangle^{1/2} = 24.5 \pm 1.7$ mm/s, $\langle v^2\rangle^{1/2} = 23.5 \pm 2.0$ mm/s, and $\langle w^2\rangle^{1/2} = 100 \pm 8$. For comparison, the synthetic data were generated using $\langle u^2\rangle^{1/2} = \langle v^2\rangle^{1/2} = \langle w^2\rangle^{1/2} = 20$ mm/s. Thus, the effect of adding noise was to increase the RMS velocities. Finally, the clustering analysis showed no clustering for both noiseless and noisy datasets (Fig. 8d), conforming to the expectation that a Gaussian stochastic process wherein particle trajectories are independent would not generate particle clustering.

Overall, the synthetic data analysis allows us to conclude that the algorithms for particle tracking, calculating the statistics of particle velocity, and quantifying particle clustering are capable of reproducing known results. Measurement noise makes tracking more difficult and leads to poor reproduction of statistics for the w component where the noise is highest. However, measurement noise does not affect the clustering analysis.

5 VoPI measurements of tracers and diatoms

5.1 Experimental methods

We used the VoPI to record the motions of tracer particles and live diatom cells in the turbulence tank. For tracer particles, silver-coated hollow glass spheres (conduct-o-fil, Potter Industries) with a median diameter of 21 µm and a mean density of 1.03 g/cm^3 (Table 3) were used. For experiments with diatoms, two different species of the genus *Coscinodiscus*

Table 3 Particle parameters computed with the following values for seawater: $\rho = 1.025$ g/cm^3 and $\nu = 1.02$ mm^2/s. For diatoms, d_p is taken to be the diameter of the diatom's cylindrical cross section

	Tracers	*C. wailesii*	*C. radiatus*
d_p (μm)	21	136	58
ρ_p (g/cm^3)	1.03	1.07	1.25
Sv_p (Low-Int)	7×10^{-4}	3×10^{-1}	2×10^{-1}
Sv_p (High-Int)	3×10^{-4}	1×10^{-1}	1×10^{-1}
St_p (Low-Int)	1×10^{-4}	4×10^{-3}	8×10^{-4}
St_p (High-Int)	5×10^{-4}	2×10^{-2}	4×10^{-3}

were used: *C. wailesii* and *C. radiatus* (Fig. 9). Cells of both *C. wailesii* and *C. radiatus* species have a cylindrical shape, but they differ in size and density. Cells were grown in L1 seawater media at 15.7 °C under 14:10 light:dark cycle and cell culture in an exponential growth phase was used in the experiments. Measurements showed (Ayres 2017) that the *C. wailesii* cells had a mean cell diameter of 136 μm and mean cell density of 1.07 g/cm^3 ($n = 30$), whereas the *C. radiatus* cells had a mean cell diameter of 58 μm and mean cell density of 1.25 g/cm^3 ($n = 31$) (Table 3).

The terminal Stokes settling velocity, the settling number, and the particle Stokes number for the different particle types are given by (Table 3):

$$V_s = \frac{[(\rho_\mathrm{p}/\rho) - 1]d_\mathrm{p}^2 g}{18\nu}, \tag{9}$$

$$\mathrm{Sv}_\mathrm{p} = \frac{V_s}{u_\eta}, \tag{10}$$

$$\mathrm{St}_\mathrm{p} = \frac{[1 + 2(\rho_\mathrm{p}/\rho)]d_\mathrm{p}^2}{36\eta^2}, \tag{11}$$

where d_p is the particle diameter and ρ_p is the particle density. These expressions assume a spherical particle whose motion relative to the fluid is characterised by a small Reynolds number, which are reasonable assumptions here. The Reynolds number based on the particle settling velocity in quiescent fluid is $(V_s d_\mathrm{p}/\nu) \leq 0.1$ for all particles.

In experiments with both tracer particles and diatoms, particles were introduced to the tank carefully and the flow–particle mixture was allowed time to come to an equilibrium state before measurements began. The following procedure was followed to achieve this. The tank was initially filled with filtered seawater until water level reached approximately 3/4 of its height. Particles were then added to the tank in the form of a suspension of tracer particles or diatom culture, filling the rest of the tank volume, and gently mixed. The culture media and the filtered seawater that initially filled the tank were from the same stock of seawater. For the tracer particles, suspensions of the tracers were agitated in a test-tube vortex mixer prior to experiments to break up aggregates. Flow was then initiated at desired turbulence level and particles were allowed to mix in the tank for 30 min before data collection started. The flow was also allowed continue between recording of replicate datasets.

Data were taken with the VoPI's measurement volume positioned 15 mm below the geometric centre of the tank. Each experiment consisted of taking images with the VoPI at 200 Hz for 20 s and repeating this procedure 20 times to generate a total of 40,000 images that were subsequently processed and analysed. We performed separate experiments for each particle type (tracers and cells of the two species of diatoms) in each mode (Low-Int and High-Int) to generate a total of six different datasets.

5.2 Experimental results

In each dataset, $O(10^4)$ particles were identified from which $O(10^3)$ tracks (e.g., Fig. 10) were found (Table 4). When comparing the RMS velocities from the SPIV measurements (Table 1) to those from VoPI measurements (Table 4), we see that the RMS velocities for tracer particles and diatoms are similar in both sets of measurements. This shows that noise in the particle's positions, which is highest in the VoPI's out-of-plane direction, is smoothed out when we calculate the particle velocity using convolution with a smoothing and differentiating kernel (Eq. (7)). From a particle–turbulence interaction point of view, this consistency in the RMS velocities across all particle types is not surprising since particle velocities are dominated by the largest scales of turbulent motion and therefore insensitive to the changes

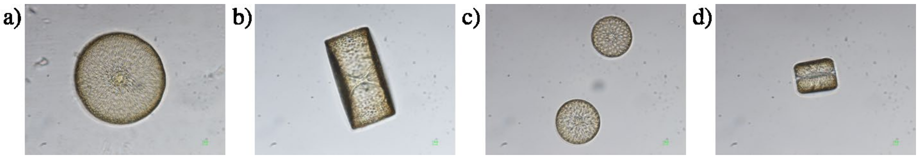

Fig. 9 Images of a *Coscinodiscus* cells. *C. wailesii*: **a** Valve (top) view and **b** Girdle (side) view. *C. radiatus*: **c** Valve (top) view and **d** Girdle (side) view during cell division

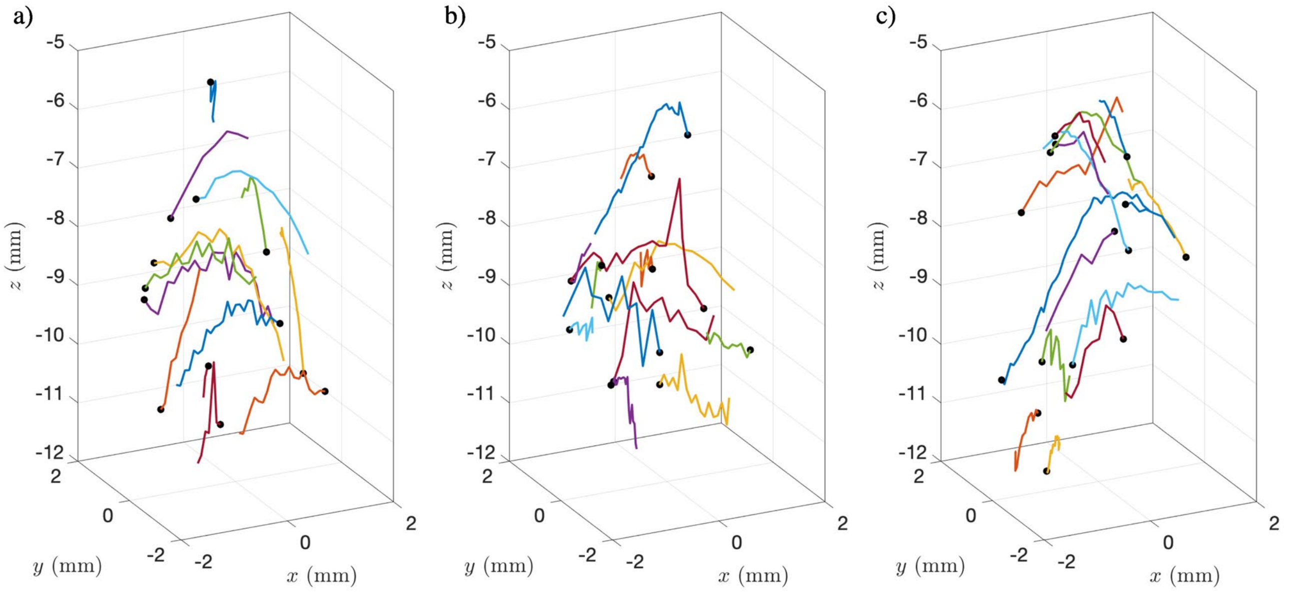

Fig. 10 Example trajectories from High-Int mode: **a** tracers, **b** *C. wailesii*, and **c** *C. radiatus*. The start of each track is marked with a black circle and the trajectories do not overlap in time

Table 4 Results of VoPI measurements of tracer particles and diatom cells in turbulence tank

	Tracers		*C. wailesii*		*C. radiatus*	
	Low-Int	High-Int	Low-Int	High-Int	Low-Int	High-Int
No. of particles	88,566	39,149	28,457	16,480	27,675	8075
No. of tracks	5351	5188	1002	1876	1280	1151
Mean velocities (mm/s) with 95% confidence intervals						
$\langle u \rangle$	−0.6 [−0.8 −0.4]	4.8 [4.3 5.4]	−0.7 [−1.0 −0.5]	2.3 [1.6 3.1]	2.4 [1.9 2.8]	4.3 [3.2 5.5]
$\langle v \rangle$	−1.0 [−1.1 −0.8]	−1.3 [−1.7 −0.9]	−1.6 [−1.9 −1.3]	−3.3 [−3.9 −2.7]	−2.0 [−2.3 −1.7]	−2.8 [−3.6 −2.0]
$\langle w \rangle$	−0.2 [−0.6 0.3]	−1.1 [−1.8 −0.4]	1.4 [0.5 2.3]	2.9 [1.9 3.9]	−0.1 [−0.8 0.6]	1.7 [0.3 3.1]
RMS velocities (mm/s) with 95% confidence intervals						
$\langle u^2 \rangle^{1/2}$	8.5 [8.3 8.6]	20.8 [20.4 21.2]	5.2 [5.0 5.4]	16.9 [16.3 17.5]	8.8 [8.4 9.1]	20.5 [19.8 21.3]
$\langle v^2 \rangle^{1/2}$	5.4 [5.2 5.5]	14.6 [14.3 14.8]	4.5 [4.3 4.8]	13.6 [13.3 13.9]	5.8 [5.6 6.0]	14.7 [14.2 15.4]
$\langle w^2 \rangle^{1/2}$	22.1 [21.1 23.1]	30.4 [29.7 31.1]	26.6 [25.0 28.1]	32.0 [31.0 33.0]	20.6 [19.8 21.5]	30.4 [28.6 32.7]

in particle size, Reynolds number, and Stokes number in these experiments.

Across different datasets in the VoPI measurements, we observe that the mean velocities of diatom cells are different to those from tracers (Table 4). The mean vertical velocity ($\langle v \rangle$) becomes more negative in the High-Int mode relative to the Low-Int mode, but this should not be interpreted as suggesting a turbulence-induced enhancement of the settling velocity because the mean horizontal velocities also show increases in magnitude. The observed differences in the mean vertical velocity could be related to particle–turbulence interactions, but will also be influenced by the structure of the mean fluid velocity in the tank, which is known to be non-stationary with $> O(1)$ mm/s changes over time (Fig. 3). Since the magnitude of the mean velocity variation is of the same order as the expected settling velocity of the particles, it is not possible to conclusively state what effects particle–turbulence interactions at the dissipation scales have on the mean settling velocity in these data. However, we can rule out the extreme enhancement of settling reported by Ruiz et al. (2004).

At the dissipation scales, we observe that both tracer particles and diatoms are likely to be found in the vicinity of other particles and cells with a higher likelihood compared to a random, uniform distribution of particles within the same volume (Fig. 11). Patchiness in the spatial

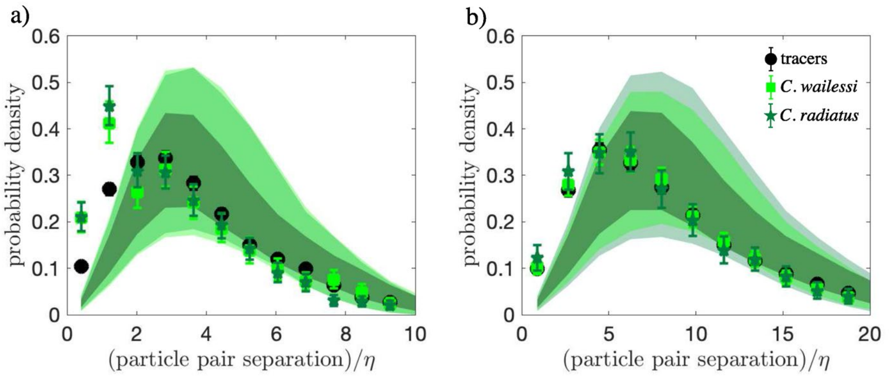

Fig. 11 Clustering data for tracers and diatoms for Low-Int mode (**a**) and High-Int mode (**b**). Symbols with 95% confidence intervals are data and the corresponding shaded regions are the 95% confidence interval bounds for the no-clustering scenario. Each data point for the diatoms data at small particle-pair separations corresponds to at least $O(10^2)$ independent observations of particle pairs

distribution of planktonic organisms at small scales has also been observed in the field (Malkiel et al. 1999, 2006), but the mechanisms that control this are not understood. In our data, tracers appear to show a weak clustering at small scales that is independent of turbulence intensity. While any clustering at this Stokes number ($\mathrm{St_p} = O(10^{-4})$) is surprising, previous experiments have reported similar behaviour (e.g., Ouellette et al. 2008).

For diatoms, clustering is weak and similar to that observed for the tracers in the High-Int mode, but stronger than that observed for the tracers in the Low-Int mode (Fig. 11). This trend in clustering is not consistent with the Stokes number (stronger clustering is observed for a lower Stokes number). Thus, other effects besides particle inertia could be causing clustering, and future work must investigate alternate mechanisms. Here, we propose three such alternate mechanisms. First, effects of particle shape could be important. Numerical simulations have shown that particles settling in turbulence can cluster even in the inertialess limit if the particle shape is non-spherical (Niazi Ardekani et al. 2017). Second, flow–particle interactions that lead to clustering in this regime may be better characterised by the settling number rather than the Stokes number. Our results would be consistent with this hypothesis, since we observe stronger clustering when $\mathrm{Sv_p}$ is closer to unity. Last, changes in cell density as a response to the turbulent flow could explain the clustering behaviour. Recent studies have shown that diatoms have the ability to modulate their buoyancy and settling speed in response to changes in light and nutrient concentrations (Du Clos et al. 2019, 2021). Under this hypothesis, our results would be consistent with the expected response: At higher energy dissipation rates, a decrease in cell density towards neutral buoyancy would decrease clustering and avoid enhanced settling via the preferential sweeping mechanism. However, further investigations are necessary before these mechanisms can be verified.

6 Conclusions

We have presented a new turbulence tank that produces homogeneous turbulence at moderate Reynolds number, yet is small enough to allow experiments with cultures of phytoplankton cells (Sect. 2). Using a volumetric particle imager (Sect. 3), we measured 3D trajectories of small, tracer particles and two species of diatoms (*C. wailesii* and *C. radiatus*) in this tank. This experimental system provides a way to systematically study small-scale interactions between diatom cells and turbulence. The results of initial experiments showed that diatom cells were more likely to be found in closer proximity to each other at dissipation scales of turbulence compared to tracer particles, but that this difference between diatoms and tracers vanished when turbulence intensity increased. This finding is consistent with several mechanisms of clustering that require further investigation, including effects of cell shape, settling number, and active regulation of cell density as a response to the ambient flow conditions.

Acknowledgements The authors would like to acknowledge funding from the U.S. National Science Foundation (OCE-1334788 to Evan A. Variano and OCE-1334365 to Lee Karp-Boss and Peter Jumars). Additionally, we would like to extend our thanks to Peter Jumars for extensive discussions at the outset of this project and for providing comments on the manuscript, Laura Mazzaro for help with designing and constructing the prototype tank, and Morteza Gharib for fruitful conversations regarding the volumetric particle imager. We also acknowledge useful comments from anonymous reviewers.

Declaration

Conflict of interest The authors declare that they have no conflict of interest.

References

Amato A, Dell'Aquila G, Musacchia F, Annunziata R, Ugarte A, Maillet N, Carbone A, Ribera d'Alcalà M, Sanges R, Iudicone D, Ferrante MI (2017) Marine diatoms change their gene expression profile when exposed to microscale turbulence under nutrient replete conditions. Sci Rep 7:3826

Armbrust EV (2009) The life of diatoms in the world's oceans. Nature 459:185–192

Arrieta J, Jeanneret R, Roig P, Tuval I (2020) On the fate of sinking diatoms: the transport of active buoyancy-regulating cells in the ocean. Philos Trans R Soc A Math Phys Eng Sci 378:20190529

Ayres S (2017) Cell density (mass per unit volume) of diatom cells and chains in relation to their size, growth, and nutritional condition. Master of science thesis, University of Maine

Bellani G, Variano EA (2014) Homogeneity and isotropy in a laboratory turbulent flow. Exp Fluids 55:1646

Borgnino M, Arrieta J, Boffetta G, De Lillo F, Tuval I (2019) Turbulence induces clustering and segregation of non-motile, buoyancy-regulating phytoplankton. J R Soc Interface 16:20190324

Bowler C, Vardi A, Allen AE (2010) Oceanographic and biogeochemical insights from diatom genomes. Annu Rev Mar Sci 2:333–365

Buchhave P, George WK, Lumley JL (1979) The measurement of turbulence with the laser-doppler anemometer. Annu Rev Fluid Mech 11:443–503

Dell'Aquila G, Ferrante MI, Gherardi M, Lagomarsino MC, d'Alcalà MR, Iudicone D, Amato A (2017) Nutrient consumption and chain tuning in diatoms exposed to storm-like turbulence. Sci Rep 7:1828

Du Clos KT, Karp-Boss L, Villareal TA, Gemmell BJ (2019) Coscinodiscus wailesiimutes unsteady sinking in dark conditions. Biol Lett 15:20180816

Du Clos KT, Karp-Boss L, Gemmell BJ (2021) Diatoms rapidly alter sinking behavior in response to changing nutrient concentrations. Limnol Oceanogr 66:892–900

Efron B, Tibshirani RJ (1993) An introduction to the bootstrap. Chapman & Hall, London

Gemmell BJ, Oh G, Buskey EJ, Villareal TA (2016) Dynamic sinking behaviour in marine phytoplankton: rapid changes in buoyancy may aid in nutrient uptake. Proc R Soc B Biol Sci 283:20161126

Gillespie DT (1996) Exact numerical simulation of the Ornstein–Uhlenbeck process and its integral. Phys Rev E 54:2084–2091

Guadayol Ò, Peters F, Stiansen JE, Marrasé C, Lohrmann A (2009) Evaluation of oscillating grids and orbital shakers as means to generate isotropic and homogeneous small-scale turbulence in laboratory enclosures commonly used in plankton studies. Limnol Oceanogr Methods 7:287–303

Kolmogorov AN (1941a) The local structure of turbulence in incompressible viscous fluid for very large Reynolds numbers. Dokl Akad Nauk SSSR 30:299–303

Kolmogorov AN (1941b) Dissipation of energy in locally isotropic turbulence. Dokl Akad Nauk SSSR 32:16–18

Malik NA, Dracos T, Papantoniou DA (1993) Particle tracking velocimetry in three-dimensional flows. Exp Fluids 15:279–294

Malkiel E, Alquaddoomi O, Katz J (1999) Measurements of plankton distribution in the ocean using submersible holography. Meas Sci Technol 10:1142–1152

Malkiel E, Abras JN, Widder EA, Katz J (2006) On the spatial distribution and nearest neighbor distance between particles in the water column determined from in situ holographic measurements. J Plankton Res 28:149–170

Malviya S, Scalco E, Audic S, Vincent F, Veluchamy A, Poulain J, Wincker P, Iudicone D, de Vargas C, Bittner L, Zingone A, Bowler C (2016) Insights into global diatom distribution and diversity in the world's ocean. Proc Natl Acad Sci USA 113:E1516–E1525

Maxey MR (1987) The gravitational settling of aerosol particles in homogeneous turbulence and random flow fields. J Fluid Mech 174:441–465

Mordant N, Crawford AM, Bodenschatz E (2004) Experimental Lagrangian acceleration probability density function measurement. Physica D Nonlinear Phenomena 193:245–251

Niazi Ardekani M, Sardina G, Brandt L, Karp-Boss L, Bearon RN, Variano EA (2017) Sedimentation of inertia-less prolate spheroids in homogenous isotropic turbulence with application to non-motile phytoplankton. J Fluid Mech 831:655–674

Ouellette NT, Xu H, Bodenschatz E (2006) A quantitative study of three-dimensional Lagrangian particle tracking algorithms. Exp Fluids 40:301–313

Ouellette NT, O'Malley PJJ, Gollub JP (2008) Transport of finite-sized particles in chaotic flow. Phys Rev Lett 101:174504

Pereira F, Gharib M (2002) Defocusing digital particle image velocimetry and the three-dimensional characterization of two-phase flows. Meas Sci Technol 13:683–694

Pérez-Alvarado A, Mydlarski L, Gaskin S (2016) Effect of the driving algorithm on the turbulence generated by a random jet array. Exp Fluids 57:20

Pope SB (2000) Turbulent flows. Cambridge University Press, Cambridge

Ragueneau O, Schultes S, Bidle K, Claquin P, Moriceau B (2006) Si and C interactions in the world ocean: importance of ecological processes and implications for the role of diatoms in the biological pump. Glob Biogeochem Cycles 20:GB4S02

Ruiz J, Macías D, Peters F (2004) Turbulence increases the average settling velocity of phytoplankton cells. Proc Natl Acad Sci USA 101:17720–17724

Salazar JPLC, de Jong J, Cao L, Woodward SH, Meng H, Collins LR (2008) Experimental and numerical investigation of inertial particle clustering in isotropic turbulence. J Fluid Mech 600:245–256

Tse IC, Variano EA (2013) Lagrangian measurement of fluid and particle motion using a field-deployable Volumetric Particle Imager (VoPI). Limnol Oceanogr Methods 11:225–238

Variano EA, Cowen EA (2008) A random-jet-stirred turbulence tank. J Fluid Mech 604:1–32

Willert CE, Gharib M (1992) Three-dimensional particle imaging with a single camera. Exp Fluids 12:353–358

Publisher's Note Springer Nature remains neutral with regard to jurisdictional claims in published maps and institutional affiliations.

Authors and Affiliations

Nimish Pujara[1,2] · **Kevin T. Du Clos**[3,4] · **Stephanie Ayres**[3] · **Evan A. Variano**[1] · **Lee Karp-Boss**[3]

✉ Nimish Pujara
npujara@wisc.edu

Evan A. Variano
variano@berkeley.edu

Lee Karp-Boss
lee.karp-boss@maine.edu

[1] Department of Civil and Environmental Engineering, University of California, Berkeley, CA 94720, USA

[2] Present Address: Department of Civil and Environmental Engineering, University of Wisconsin-Madison, Madison, WI 53706, USA

[3] School of Marine Sciences, University of Maine, Orono, ME 04473, USA

[4] Present Address: Institute for Ecology and Evolution, University of Oregon, Eugene, OR 97403, USA